NEUROSCIENCE

Multifunctional fibers enable modulation of cortical and deep brain activity during cognitive behavior in macaques

Indie C. Garwood[1], Alex J. Major[2], Marc-Joseph Antonini[3,4], Josefina Correa[5], Youngbin Lee[3,6], Atharva Sahasrabudhe[3,4,7], Meredith K. Mahnke[2], Earl K. Miller[2,5]*†, Emery N. Brown[1,2,5,8,9,10]*†, Polina Anikeeva[3,4,5,6]*†

Copyright © 2023 The Authors, some rights reserved; exclusive licensee American Association for the Advancement of Science. No claim to original U.S. Government Works. Distributed under a Creative Commons Attribution NonCommercial License 4.0 (CC BY-NC).

Recording and modulating neural activity in vivo enables investigations of the neurophysiology underlying behavior and disease. However, there is a dearth of translational tools for simultaneous recording and localized receptor-specific modulation. We address this limitation by translating multifunctional fiber neurotechnology previously only available for rodent studies to enable cortical and subcortical neural recording and modulation in macaques. We record single-neuron and broader oscillatory activity during intracranial GABA infusions in the premotor cortex and putamen. By applying state-space models to characterize changes in electrophysiology, we uncover that neural activity evoked by a working memory task is reshaped by even a modest local inhibition. The recordings provide detailed insight into the electrophysiological effect of neurotransmitter receptor modulation in both cortical and subcortical structures in an awake macaque. Our results demonstrate a first-time application of multifunctional fibers for causal studies of neuronal activity in behaving nonhuman primates and pave the way for clinical translation of fiber-based neurotechnology.

INTRODUCTION

Studying the relationship between neural activity and behavior is a cornerstone of systems neuroscience research and an essential step in the development of therapies for brain disorders. Neural encoding of behavioral information occurs across a multitude of timescales from millisecond single-neuron activity (*1*, *2*) and coordinated activity from populations of neurons (*3*) to low-frequency local field potential (LFP) oscillations (*4*) and network communication across distant brain areas (*5*). State-space and generalized linear models provide a powerful, flexible approach to decoding behavioral information from time-varying neurophysiology measurements (*1*, *6*–*10*). Together, advancements in neural recording and decoding have enabled breakthroughs in brain machine interfaces for controlling prosthetic limbs and other assistive devices. However, purely observational approaches fall short from establishing causal rather than correlative associations between brain activity and the flexible computations that underly behavior. Furthermore, the ability to perturb neural activity is critical in developing effective treatments for neurological and mental illnesses (*11*, *12*). For example, recording the effects of activating or inhibiting potential seizure foci in epilepsy patients would provide key evidence for resection surgeries (*13*).

While cell-type–specific modulation of genetically engineered receptors is a powerful neuroscience research tool (*14*), genetic alterations are challenging in translational models such as nonhuman primates (NHPs) (*15*). Furthermore, clinical implementation of transgene-mediated neuromodulation is now infeasible. In contrast, clinically accepted intracranial drug delivery enables modulation of specific receptors and, combined with electrophysiology measurements, can establish causal links between receptor function and neural encoding (*16*–*19*). Although routine in rodents, intracranial drug delivery in NHPs is hampered by a limited toolbox, which includes iontophoresis and pressure injection probes. Iontophoresis is limited to polar molecules, prone to artifacts, and reliant on fragile glass pipettes (*20*). Pressure injection probes to date have used rigid capillaries of steel or glass with diameters of 200 to 420 μm (*21*–*25*), and probes that include more than a single electrode have diameters of ≥230 μm.

Multifunctional neurotechnology with smaller dimensions and softer materials (e.g., polymers and hydrogels) has the potential to reduce tissue damage and foreign body responses, enabling longer-term experiments (*26*–*30*). While the past decade of research into flexible bioelectronic interfaces has yielded a vast array of tools for rodent studies (*31*–*34*), few technologies have been translated to NHPs, a model essential for causal studies of higher cognitive functions (*33*, *35*). Technology development for NHPs has occurred almost exclusively in the private sector, with limited adoption of recent materials advances (*24*, *25*).

Here, we present miniature and flexible electrofluidic neural interfaces for NHPs based on multifunctional fibers produced via thermal drawing at a scale of meters (*36*–*39*). This process is uniquely suited for translation of tools from rodents to NHPs. Our multifunctional fiber–based neural interface for NHPs

[1]Harvard-MIT Division of Health Sciences and Technology, Massachusetts Institute of Technology, Cambridge, MA, USA. [2]The Picower Institute for Learning and Memory, Massachusetts Institute of Technology, Cambridge, MA, USA. [3]Research Laboratory of Electronics, Massachusetts Institute of Technology, Cambridge, MA, USA. [4]McGovern Institute for Brain Research, Massachusetts Institute of Technology, Cambridge, MA, USA. [5]Department of Brain and Cognitive Sciences, Massachusetts Institute of Technology, Cambridge, MA, USA. [6]Department of Materials Science and Engineering, Massachusetts Institute of Technology, Cambridge, MA, USA. [7]Department of Chemistry, Massachusetts Institute of Technology, Cambridge, MA, USA. [8]Department of Anesthesia, Critical Care, and Pain Medicine, Massachusetts General Hospital, Boston, MA, USA. [9]Institute for Medical Engineering and Sciences, Massachusetts Institute of Technology, Cambridge, MA, USA. [10]Department of Anaesthesia, Harvard Medical School, Boston, MA, USA.
*Corresponding author. Email: anikeeva@mit.edu (P.A.); enb@neurostat.mit.edu (E.N.B.); ekmiller@mit.edu (E.K.M.)
†These authors contributed equally to this work.

Downloaded from https://www.science.org at Massachusetts Institute of Technology on October 26, 2023

comprises four tungsten microelectrodes and two microfluidic channels integrated within a poly(etherimide) (PEI) cladding with outer diameter of 187.1 ± 2.5 μm, 18 to 55% smaller than existing multielectrode alternatives (*21*–*23*).

We applied multifunctional fibers to deliver microinfusions of γ-aminobutyric acid (GABA) to the premotor cortex of a rhesus macaque while simultaneously recording single-unit and LFP activity. Intracortical GABA infusions have been shown to inhibit neurons and alter neuronal computations (*40*–*42*). The duration of GABA-mediated inhibition can be adjusted from the order of seconds to minutes by varying the volume infused, which enables within-session comparisons of single-neuron activity before and after local inhibition (*41*). Because the premotor cortex is known to be involved in multiple cognitive processes, including working memory (*43*, *44*), we leveraged multifunctional fibers to explore the effects of local inhibition on encoding of working memory by single-unit activity patterns and LFPs. Characterizing the dynamics of these multilevel neuromodulation datasets demanded innovation in neural data analysis methods, including expansion of state-space generalized linear models (SS-GLMs) for point processes. Application of SS-GLM formalism afforded rigorous quantification of the effects of neuromodulation with temporal resolution surpassing that of standard neural data analysis methods, revealing how task-evoked neural activity is reshaped by local inhibition. Last, we demonstrate that the probes are capable of recording and modulating task-related activity in the putamen, a deep brain structure known to be involved in reward-mediated learning and working memory (*45*, *46*). Despite their expanded functionality, multifunctional fibers readily integrate into existing experimental setups in laboratories using off-the-shelf NHP neurotechnologies. Consequently, we envision that these fiber-based tools will empower NHP neuroscience, enabling causal studies of the role of receptors in circuit function and high-level cognitive behaviors. Furthermore, our results highlight the safety and utility of fiber-based tools for translational research.

RESULTS

Multifunctional fibers for drug delivery and electrophysiology

Although multifunctional fibers have been extensively applied for recording and modulation of neural activity in freely behaving rodents, the potential of this platform for multimodal neural interrogation in behaving NHPs remained to be harnessed. Here, we applied thermal drawing to create fibers capable of simultaneous drug delivery and electrophysiology recording in NHPs (Fig. 1A). During thermal drawing, a macroscale preform is heated and pulled into a fiber with equivalent cross-sectional geometry but microscale dimensions (Fig. 1B) (*36*–*39*). We used PEI, a high-performance thermoplastic, as the main structural component of our fiber. To incorporate 25-μm tungsten electrodes into the fiber, we applied convergence drawing (*36*). The diameter of the fiber was tuned by adjusting the relative rate that the preform was fed into the furnace versus the pulling rate of the fiber, producing 8 m of fiber with diameter tuned between 150 and 200 μm (fig. S1, A to C).

The devices were fabricated from 7.0 ± 0.3–cm sections of fiber with 187.1 ± 2.5–μm diameter (Fig. 1, C and D), approximately 25 times longer than those used for devices applied in rodent brains (fig. S1D) (*36*). The fibers included four 25-μm tungsten microelectrodes and two microfluidic channels of (49.9 ± 0.7) μm by (62.4 ± 0.8) μm (Fig. 1, D and E). The multifunctional fibers were outfitted with modular backends that used commercial electrode connectors (see Materials and Methods) and 304–μm–inner diameter (ID) and 457–μm–outer diameter (OD) stainless steel cannulas for the fluidic interface. In addition to fiber length, stainless steel reinforcement tubes (OD = 635 μm) permitted interfacing with standard microdrive holders (Fig. 1F). Up to eight probes connected to the same backend can be assembled into microdrives, with independent fluidic interfaces for each probe, enabling independent depth control of multiple fibers for broad-scale interrogation of neural activity (fig. S1, E and F).

The choice of materials and backend interface was informed by the need for thorough sterilization of the devices. The relatively high glass transition temperature (T_g = 217°C) of PEI allowed the fiber-based devices to be autoclaved without deforming while encasing the backend electrode interface in medical epoxy protected the electrical components. The impedance magnitude ($|Z|$) of the integrated electrodes did not change significantly after autoclave sterilization (before $|Z|$ = 223.9 ± 36.6 kilohms and after $|Z|$ = 206.7 ± 22.9 kilohms; Fig. 1G). Accurate infusion of nanoliter volumes at rates of 10 to 100 nl/min was achieved with 7.0 ± 0.3–cm–long fibers, with measured infusion rates matching those set by an infusion pump (Fig. 1H). This resulted in accurate infusions, with mean absolute error between the actual and expected infusion volume of 1.77 nl at 50 nl/min. The stiffness of the fibers was 45.53 ± 1.14 N/m in the frequency range of respiration and heartbeat for NHPs (Fig. 1I), which is significantly lower than that of a stainless steel cannula with dimensions comparable to fluid infusion devices used in NHP research (OD = 203 μm, ID = 50 μm, and stiffness = 180.99 ± 0.22 N/m).

Simultaneous intracortical drug delivery and neural activity recordings

To illustrate simultaneous pharmacological modulation and electrophysiological monitoring of neuronal activity in NHPs, we applied multifunctional fibers to record single-unit and LFP activity while delivering GABA in the premotor cortex. The waveforms from neuronal action potentials were recorded across the four electrodes, providing four observations of the same putative single unit (Fig. 2, A and B). Single units were isolated by clustering the principal components of waveforms across the four electrodes (fig. S2), which were stable between the baseline and recovery phases. The ability to record neural activity before, during, and after the infusions enabled tracking of putative single-unit activity in response to intracranial GABA delivery [signal-to-noise ratio (SNR) baseline = 3.08 [0.82, 26.15], SNR during = 5.42 [1.31, 16.27], and SNR recovery = 9.61 [1.26, 24.42]; median [95% confidence intervals]; Fig. 2C].

In accordance with GABA's role as an inhibitory neurotransmitter, we observed inhibition of single-unit activity following 5-min infusions of 100 mM GABA at 10 and 50 nl/min (*42*). Depending on the volume of GABA delivered (50 nl over 5 min or 250 nl over 5 min), we were able to cause inhibition of firing activity for both short (unit 2, 50 nl: 1.78 [1.38, 1.85] min) and long durations (unit 1, 250 nl: 12.63 [8.10, 13.21] min; unit 2, 250 nl: 29.03 [26.25, 29.12] min), followed by recovery of firing rates similar to or exceeding baseline rates (Fig. 2, D and E). Firing rates were estimated using a state-space point process model (see Materials and

Downloaded from https://www.science.org at Massachusetts Institute of Technology on October 26, 2023

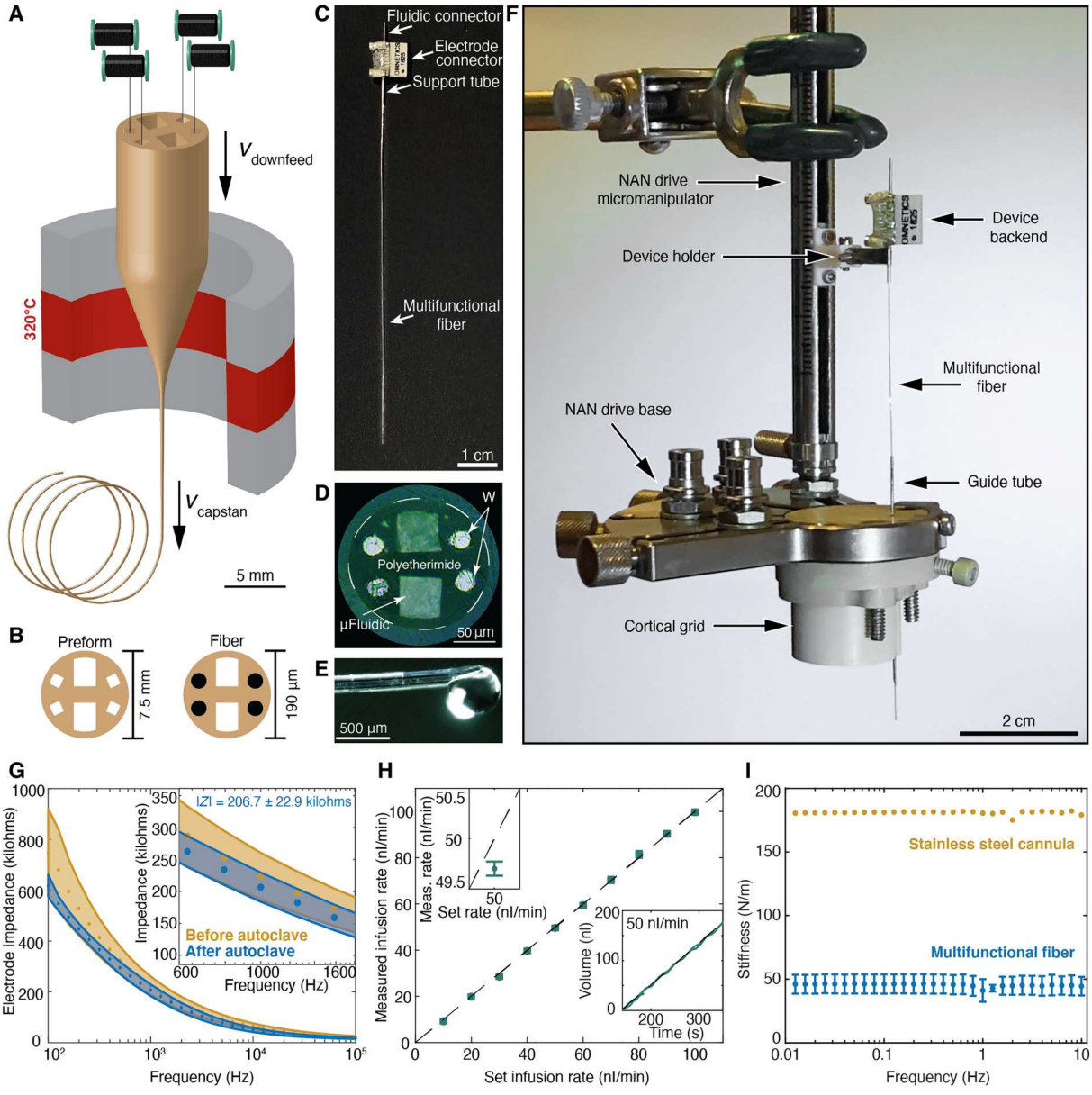

Fig. 1. Fabrication of multifunctional fiber–based probes. (**A**) The fiber preform was heated to 320°C and pulled downward by a capstan. The cross-sectional area of the fiber was set by the relative velocity of the downfeed ($v_{downfeed}$) and capstan ($v_{capstan}$). Tungsten (W) microwires were incorporated into the fiber via convergence (Methods). (**B**) The resulting fiber (d_{fiber} = 187.1 ± 2.5 µm) has the same cross-sectional geometry as the preform ($d_{preform}$ = 7.5 mm). (**C**) Each fiber is outfitted with an electrode connector, a stainless steel fluidic connector, and a stainless steel support tube. (**D**) Cross section of a fiber embedded in epoxy. Dashed line marks the outside circumference of the fiber. (**E**) Microfluidic injection via the fiber. (**F**) The devices assembled in a cortical grid with a commercial microdrive. (**G**) Electrode impedance spectrum (inset, 600 to 1600 Hz). The mean impedances ± SE before (yellow) and after (blue) autoclave sterilization. (**H**) Microfluidic infusion rates at set rates between 10 and 100 nl/min. Each point shows the measured infusion rate and 95% confidence intervals (top inset, infusion rate at 50 nl/min; bottom inset, the infusion profile at a steady state). (**I**) Stiffness of fibers (n = 3) and stainless steel cannula (inner diameter = 51 µm and outer diameter = 203 µm) across the frequency ranges of locomotion, respiration, and heart rate.

Methods) (*7*). Down states were defined as periods where the firing rate was below the minimum baseline firing rate for at least 10 consecutive seconds. Confidence intervals of 95% for firing rates, down state times, and down state durations were estimated with Monte Carlo (see Materials and Methods). The onset of down states varied between neurons. In this recording, the firing rate of unit 1 was not significantly reduced following the 50 nl of GABA infusion, while unit 2 was significantly inhibited 3.83 [3.82, 3.90] min following the beginning of the infusion. During the second infusion, unit 1 was significantly inhibited 1.37 [1.30, 2.31] min after beginning of the second infusion, while unit 2 was inhibited after just 0.65 [0.64, 0.73] min. The variation in the response to GABA between neurons may reflect variation in GABA receptor expression, cellular excitability, and synaptic input from other neurons (*47*, *48*).

Downloaded from https://www.science.org at Massachusetts Institute of Technology on October 26, 2023

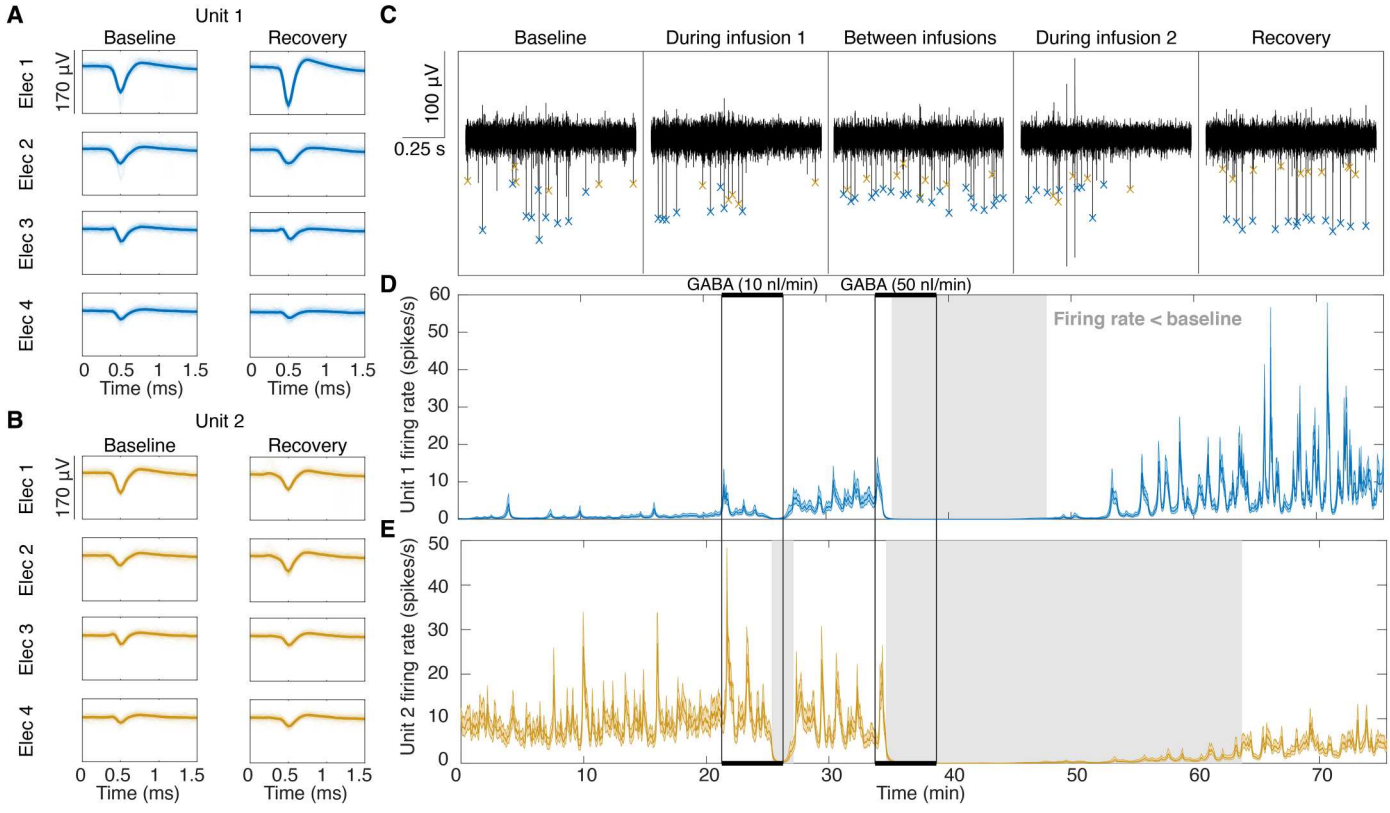

Fig. 2. Multifunctional fibers record the effects of intracortical GABA delivery on single-unit activity. (**A** and **B**) The waveforms of units 1 and 2 recorded across four electrodes of the same probe were stable in shape and amplitude before and after 100 mM GABA infusions. (**C**) The noise floor was consistent before, during, and after GABA infusions at 10 nl/min (infusion 1) and 50 nl/min (infusion 2). Blue and yellow markers correspond to units 1 and 2, respectively. (**D** and **E**) Firing rate was modeled with a state-space point process model (see Materials and Methods). Confidence intervals of 95% for the estimated rate are shown with the blue and yellow shaded areas. Periods where the estimated firing rate was lower than the minimum baseline firing rate are shaded in gray. Infusion periods are indicated with black rectangles. (D) The mean firing rate of unit 1 was 0.82 [0.78, 0.89] spikes/s before the first GABA injection, decreased below baseline for 12.63 [8.10, 13.21] min following the GABA injection at 50 nl/min, and then increased to 6.05 [5.30, 6.30] spikes/s. (E) The mean firing rate of unit 2 was 9.10 [9.01, 9.34] spikes/s before the first GABA injection, decreased below baseline for 1.78 [1.38, 1.85] min following the injection at 10 nl/min and for 29.03 [26.25, 29.12] min following the injection at 50 nl/min, and then recovered to 3.87 [3.48, 4.06] spikes/s.

Overall, 9 of the 10 recorded neurons had significantly decreased mean firing rate in the 10 min following GABA infusions, with a subsequent increase in firing rate 20 min after the end of the infusion (fig. S3). Thus, to compare neurophysiology over time, we define four periods: (i) the baseline period, before any fluid was delivered; (ii) the infusion period(s), during intracranial microinfusion(s); (iii) the inhibition period, 10 min following the last microinfusion; and (iv) the recovery period, greater than 20 min after microinfusion(s).

We also observed changes in the oscillatory structure of the LFP between the baseline and inhibition periods, which reflects local changes in neuronal population activity (*49*). Figure 3A shows the spectrogram of LFP recorded in the same session reported in Fig. 2. We used the fitting oscillations and one-over-F (FOOOF) algorithm to characterize LFP spectra (*50*), which models a given power spectral density (PSD; in decibels) as a sum of an aperiodic exponential decay component and periodic oscillation peaks (see Materials and Methods). The aperiodic component has a broadband offset and rate of exponential decay that characterizes the decrease in power with increasing frequency, a common feature of neural spectra (*49*, *50*). We found dominant oscillatory peaks in three frequency ranges across four recordings: 11 to 17 Hz [mean center frequency (MCF): 13.46 [13.35, 13.61] Hz], 27 to 35 Hz (MCF: 29.73 [29.64, 29.82] Hz), and 47 to 62 Hz (MCF: 54.59 [54.03, 55.04] Hz; Fig. 3C). Note that these ranges, estimated from the unsupervised FOOOF algorithm, correspond to the canonical alpha, beta, and gamma frequency ranges. We found that, during the inhibition period following intracranial GABA infusion, there was a significant decrease in mean peak LFP power in the 27- to 35-Hz and 47- to 62-Hz ranges (Δ_{27-35} = −1.09 [−1.44, −0.73] dB and Δ_{47-62} = −0.55 [−0.86, −0.28] dB; Fig. 3, B to D) and an increase in mean peak power in the 5- to 8-Hz, 17- to 25-Hz, 35- to 47-Hz, and 70- to 100-Hz ranges (Δ_{5-8} = 0.35 [0.03, 0.62] dB, Δ_{17-25} = 0.55 [0.31, 0.81] dB, Δ_{35-47} = 0.21 [0.03, 0.50] dB, and Δ_{70-100} = 0.16 [0.08, 0.29] dB; Fig. 3, C and D). We found a decrease in the offset of the aperiodic decay (Δ_{offset} = −0.02 [−0.03, −0.01] dB) and an increase in the exponent ($\Delta_{exponent}$ = 0.03 [0.01, 0.04] dB; Fig. 3E), which is consistent with previous observations that an increased rate of exponential decay in cortical LFP power reflects neuronal inhibition (*51*). Overall, GABA reduced LFP power, particularly in the 27- to 35-Hz and 47- to 62-Hz frequency bands (Fig. 3F).

Downloaded from https://www.science.org at Massachusetts Institute of Technology on October 26, 2023

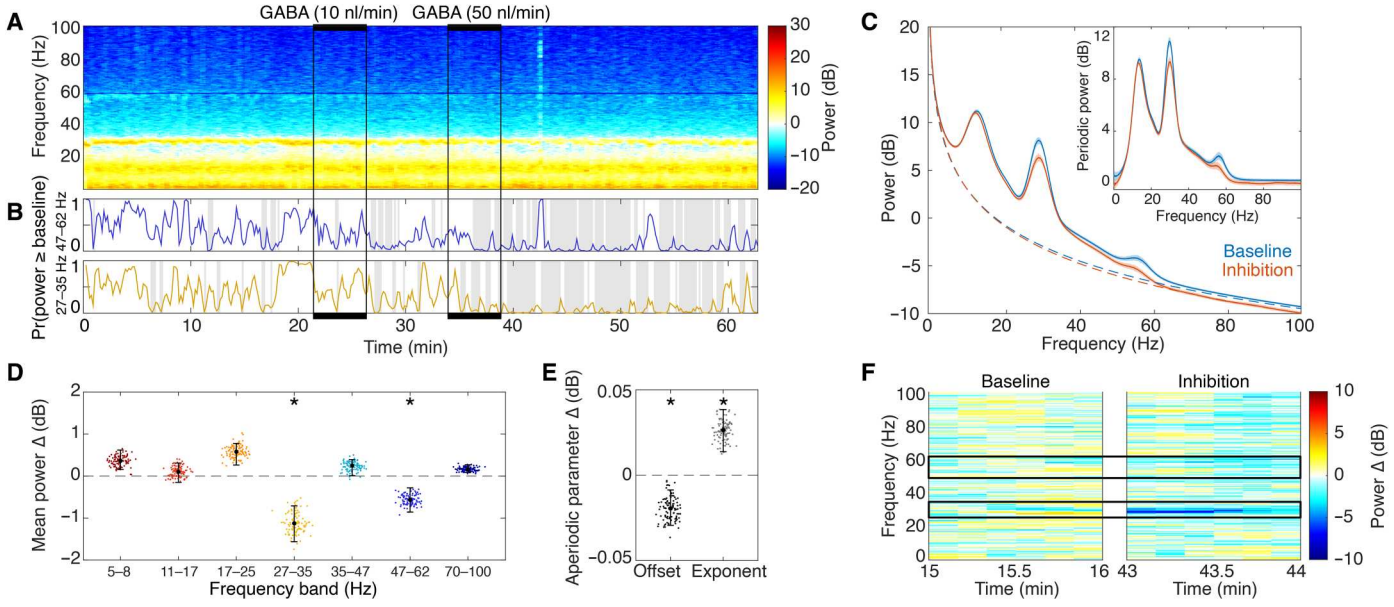

Fig. 3. Intracortical GABA delivery alters the oscillatory structure of LFPs. (**A**) The multitaper spectrogram calculated from the LFP activity. (**B**) The probabilities that peak power in the 27- to 35-Hz (yellow) and 47- to 62-Hz (blue) bands is greater than or equal to the peak power before 100 mM GABA was delivered [Pr(power ≥ baseline)]. Periods where this probability is below 0.1 are shaded in gray. (**C**) The mean and 95% confidence intervals of 100 bootstrap samples of the mean spectral power calculated from 10-min periods before (blue) and after (red) GABA across four infusion sessions. The dashed lines show the mean aperiodic component before (blue) and after (red) GABA. Inset: The mean and 95% confidence intervals for the spectral power minus the aperiodic component. (**D**) One hundred bootstrap estimates of the change in mean peak power in the 10 min before the first GABA infusion versus the 10 min after the last GABA infusion across four infusion sessions. Black markers represent median, and the error bars represent 95% confidence intervals. Asterisks indicate bands where the change is significantly greater than during control infusion or no-infusion experiments (fig. S5). (**E**) The mean estimated exponent of the aperiodic component was increased following GABA infusion. The aperiodic offset decreased less during GABA experiments compared to control experiments (fig. S5). (**F**) Spectrogram segments of baseline and inhibition periods, where power Δ is the power compared to mean baseline power in decibels.

We controlled for the effect of the infusion by comparing the effect of GABA to saline or artificial cerebrospinal fluid (aCSF) and to recordings without infusions (figs. S4 and S5). Recordings without microinfusions were separated into two periods: (i) baseline, 0 to 10 min after the beginning of the recording; and (ii) after baseline, greater than 13 min following the beginning of the recording. We found that the SNR was stable across all single-unit recordings (ratio of SNR after to SNR before = 1.12 [0.89 to 1.32]; figs. S4 and S5). In contrast to GABA, the firing rate in saline or no-infusion experiments either stayed the same or increased from baseline (mean firing rate ratio across all neurons during inhibition period versus baseline for GABA = 0.28 [0.11, 0.50], saline = 0.94 [0.86, 1.03], and no infusion = 1.40 [1.14, 1.71]) (figs. S4 and S5). Compared to control or no infusions, changes in LFP of 27- to 35-Hz and 47- to 62-Hz oscillations were significantly greater in magnitude following GABA infusions (fig. S5). The aperiodic exponent of LFP spectral power was significantly increased following GABA infusions compared to control and no-infusion conditions. The aperiodic offset decreased across each experimental condition, and the decrease was significantly greater during control infusions. We did not observe trends related to session order that could explain the differences between GABA and control sessions (fig. S6).

Modulation of cognitive task encoding

We hypothesized that, in addition to locally reducing firing rates and altering LFP oscillations, intracranial GABA infusions may locally alter cognitive encoding in the premotor cortex (Fig. 4A) (*18*, *52*). To test this hypothesis, we recorded neural activity while the NHP performed a delayed match–to–sample (DMS) working memory task (Fig. 4, B and C) (*43*, *53*, *54*). In each trial, after fixating on the center of a screen, the NHP was presented with one of three images for 1 s (sample phase). The image then disappeared for 1 s (delay phase). Then, two images appeared on the screen in the top right and bottom left corners, and the NHP saccaded to one of the images (match phase). If the NHP selected the image presented during the sample phase, then they were rewarded with a juice pulse (reward phase). If not, the trial ended with no reward.

Consistent with previous studies of working memory (*43*, *44*), we observed that the single-unit firing rate in the premotor cortex varied consistently within trials (Fig. 4D and figs. S7, S9, and S10). We compared the peristimulus time histogram (PSTH) before, during, and after GABA and observed changes in both firing rate and task-evoked neuronal activity (fig. S7). To capture the temporal dynamics of these changes, we applied a SS-GLM (*8*, *55*). Compared to standard methods of calculating average firing rate from 100-ms bins and multiple trials (i.e., the PSTH), the SS-GLM quantifies neural activity with millisecond and single-trial resolution. In our analysis, we separated each trial into 50 evenly spaced subphases and investigated how the firing rate varied between each subphase. We modeled single-unit activity as a point process, where the instantaneous firing rate varied as a function of the firing history of the single unit and the trial subphase (see Materials and Methods). The SS-GLM captured firing dynamics within a trial that were

Downloaded from https://www.science.org at Massachusetts Institute of Technology on October 26, 2023

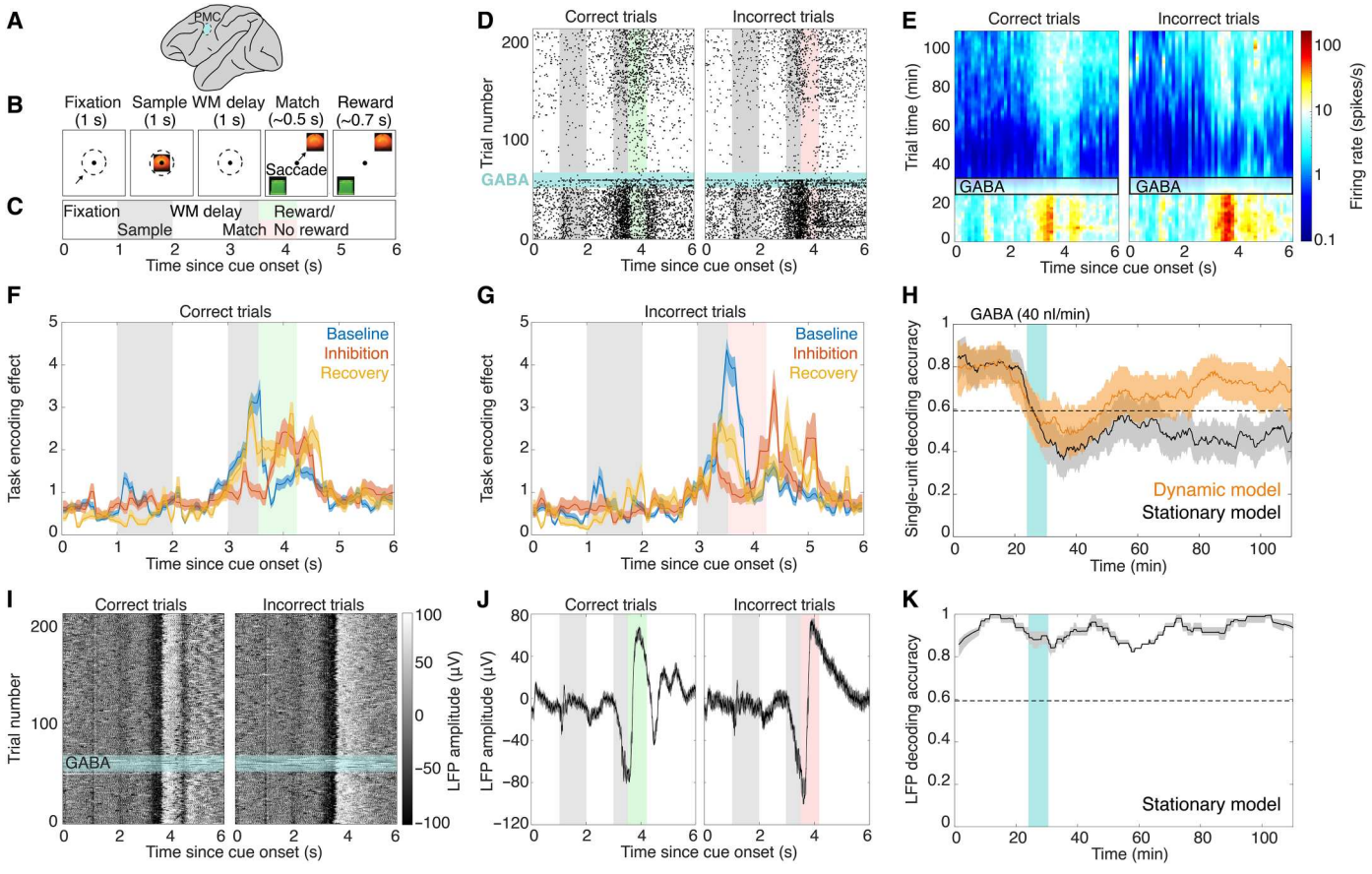

Fig. 4. Intracranial GABA infusions alter neural encoding during a working memory task. (**A**) Multifunctional fibers were implanted in the premotor cortex. PMC, premotor cortex; WM, working memory. (**B**) During the delayed match–to–sample (DMS) working memory task, the NHP saccaded to the choice that matched the sample, and, if correct, juice was dispensed. (**C**) Task color legend for (D), (F), (G), and (J). (**D**) Raster plots of single-unit activity during correct and incorrect trials. The cyan shading marks GABA infusion (100 mM, 40 nl/min). (**E**) SS-GLMs were used to estimate the firing rate within and across trials. The horizontal rectangle indicates GABA infusion. (F and G) The task encoding effect (a scaling factor for within-trial firing rate) during correct (F) and incorrect (G) trials varied between the baseline (blue), inhibition (red), and recovery (yellow) periods. (**H**) Correct versus incorrect trial mean decoding accuracy using SS-GLM models of single-unit activity (orange line; orange shading marks 95% confidence intervals). The dashed line indicates the null decoding accuracy, the vertical cyan bar marks GABA infusion, and the black line indicates decoding accuracy using stationary models trained on pre-GABA single-unit activity (gray shading, 95% confidence intervals). (**I**) LFP amplitude across trials. The cyan shading marks GABA infusion. (**J**) An autoregressive model with trial covariates characterized LFP amplitude within trials. The black line and gray shading indicate the mean and 95% confidence intervals. (**K**) Correct versus incorrect trial decoding accuracy using LFP observations was above null throughout the experiment.

driven by innate properties of the neuron, such as refractory period, and those that were driven by task encoding (Fig. 4E and fig. S8). Each trial had a unique set of trial subphase coefficients, which were modeled as latent state variables that vary smoothly between sequential trials. The latent state process characterized how firing rate and task encoding changed across trials. Overall, the SS-GLM provided a unified, high-resolution model for characterizing changes in firing rate within and across trials. Trials were ordered sequentially, and the model was estimated from odd (training) trials, while goodness of fit was assessed from even (test) trials (fig. S8). We found that trial subphase was a significant predictor of firing rate for 28 of the 36 single units recorded across 12 recording sessions (likelihood ratio test, $P < 0.05$; see Materials and Methods and fig. S9).

We then investigated whether task-evoked activity varied between trial variants (left versus right saccades, sample ID, choice ID, and correct versus incorrect trials). We separately estimated models from training trials belonging to each trial variant and then compared the difference in task-evoked activity between each variant (fig. S10). Figure 4 (D to G) describes a unit for which task-evoked activity varied most significantly between correct versus incorrect trials. GABA delivery reduced the unit's firing rate and restructured its task encoding (Fig. 4D). The SS-GLM provided a quantitative characterization of these observations (Fig. 4E). Together, the multifunctional fibers and SS-GLM provided the opportunity to investigate how single-unit task encoding changed following local inhibition. By factoring out the estimated trial average firing rate, the variation in firing rate due to the task (the task encoding effect) could be isolated and compared between the baseline, inhibition, and recovery periods (Fig. 4, F and G). Before GABA infusion, this unit exhibited an increase in firing rate at the beginning of the sample phase in both correct and incorrect trials. Then, the firing rate gradually increased from the delay phase to the decision point. During correct trials, the firing rate rapidly dropped when juice was dispensed. During incorrect trials, the firing rate continued to rise before decreasing in the middle of the expected reward

Downloaded from https://www.science.org at Massachusetts Institute of Technology on October 26, 2023

phase. Thus, before GABA, this unit encoded information across multiple trial phases, including the presence or absence of reward. Because the premotor cortex has a role in saccades (*56*), we tested whether the variation in firing rate was related to saccades rather than reward. We found less variation in firing rate due to saccades that occurred outside of the match/reward period compared to the variation that occurred during the reward period (fig. S10), indicating that the firing rate of this unit reflected reward-related information.

We found that local GABA infusions altered the task encoding effect: 4.0 min into the GABA infusion, there was a significant reduction in firing rate, but this inhibitory effect was not uniform across subphases. As the effect of the GABA infusion wore off, there was an increase in firing rate, particularly during the match and reward phases. The increase in firing rate at the beginning of the sample phase was lost during the inhibition period and did not recover. As a result, 65 to 80 min after GABA, the 95% confidence intervals of the task encoding effect had 55.0 and 62.5% overlap with the baseline task encoding effect for correct and incorrect trials respectively, indicating incomplete recovery of task-encoded activity.

We investigated how changes in task encoding caused by local GABA infusions affected the ability to decode behavioral information from single-unit activity (Fig. 4H). We decoded correct versus incorrect trials by comparing the deviance of the data observed during test trials from two SS-GLMs estimated from correct or incorrect training trials. Before GABA, it was possible to decode whether test trials were correct or incorrect with 80 [72, 87]% accuracy from the activity of one single unit alone, which is significantly above the null decoding accuracy of 59% (see Materials and Methods). As the task-encoded activity of the neuron shifted in response to GABA, the ability to reliably decode correct versus incorrect trials dropped below the null decoding accuracy (decoding accuracy during the inhibition phase = 49 [38, 61]%). The lower 95% confidence interval of the decoding accuracy first passed above the null decoding accuracy 43.3 min after the end of the GABA infusion, when the trial average firing rate was 16.1 [7.4, 35.8]% of the baseline levels and task encoding remained significantly different from baseline. Thus, despite persistent changes in the task-encoded activity, there was sufficient information encoded in the signal to distinguish correct versus incorrect trials above chance. We compared the SS-GLM to a standard GLM with stationary trial phase coefficients estimated from pre-GABA trials. The stationary model did not capture the return of reward encoding (Fig. 4H), highlighting the need for dynamic models to account for changes in neuronal encoding following neuromodulation.

We found that local GABA delivery had a contrasting effect on encoding of task-related LFP activity. First, task-related LFP activity was relatively stable throughout the experiment (Fig. 4I), despite changes in the oscillatory structure of the LFP (Fig. 3). We modeled the relationship between LFP amplitude and trial phase using an autoregressive model with trial phase covariates. A model with stationary trial phase coefficients was sufficient to capture the temporal structure of LFP-evoked activity throughout the experiment (fig. S12). The mean and 95% confidence intervals of the event-related potentials for correct and incorrect trials are shown in Fig. 4J. We found that LFP was a reliable marker of whether a trial was correct or incorrect (94 [93, 96]% accuracy before GABA; Fig. 4K). In contrast to single-unit activity, the decoding accuracy from LFP was stable during and following local GABA delivery (89 [86, 92]% and 89 [86, 91]% accuracy during the infusion and inhibition phases, respectively; Fig. 4K and fig. S13).

While we did not anticipate changes in behavior due to the submicroliter GABA infusions into premotor cortex (*18*, *19*), we assessed whether changes in neurophysiology caused by GABA affected task performance across several metrics. We compared task accuracy, response time, trial completion rate, and action selection bias before and after GABA (fig. S12 and Materials and Methods). We did not observe any consistent changes in behavior due to GABA microinfusions compared to control conditions.

Intrastriatal modulation of neural activity and cognitive task encoding

Given that therapeutic and diagnostic neuromodulation is most frequently performed in subcortical brain regions, we sought to demonstrate the utility of fiber neurotechnology in a deep brain structure. The unrestricted fiber length was leveraged to record the effect of intrastriatal GABA delivery on single-unit and LFP activity in the putamen (Fig. 5A), a subcortical structure with multiple functions, including processing reward (*45*, *46*). Because of the proximity of the putamen to important regulatory centers, we infused a smaller volume of GABA as compared to the cortical recordings (putamen, 56 nl total; premotor cortex, 222.8 ± 27.8 nl total). As in the cortical recordings, single-unit activity was recorded before and after GABA delivery (Fig. 5B). This unit's task-encoded activity varied between correct and incorrect trials, particularly during and immediately following the reward phase (Fig. 5, C to F). Additional putamen recordings confirmed the presence of reward-evoked single-unit activity, as well as the presence of previously reported positive spikes (fig. S15) (*57*), highlighting the value of electrophysiology signatures for spatially localizing intracranial infusions. As in the premotor cortex analysis, the SS-GLM characterized how task-encoded activity varied following local GABA delivery (Fig. 5D). There was a decrease in trial average firing rate during the GABA infusion (firing rate in the trial preceding GABA = 8.27 [7.59, 8.99] spikes/s and firing rate in the trial following GABA = 4.76 [4.36, 5.22] spikes/s), followed by an increase in firing rate in specific trial phases (Fig. 5D). Figure 5 (E and F) characterizes how the task encoding effect varied during the baseline, after GABA, and recovery period. The most significant changes included an increase in firing rate following the reward phase in incorrect trials during the recovery period. This manifested as a greater difference between correct and incorrect trials and an increase in single-unit decoding accuracy during the recovery period.

Similar to the premotor cortex recordings, there was a modulation of LFP oscillatory content following GABA delivery. Using the FOOOF algorithm, we found that there was a significant decrease in the 11- to 15-Hz, 27- to 32-Hz, and 54- to 60-Hz bands ($\Delta_{11–15}$ = −1.05 [−1.72, −0.29] dB, $\Delta_{27–32}$ = −3.56 [−4.29, −2.71] dB, and $\Delta_{54–60}$ = −1.5 [−1.72, −0.29] dB) and a significant increase in the 76- to 85-Hz band ($\Delta_{76–85}$ = 0.33 [0.03, 0.63] dB; Fig. 5, H and I). In contrast to the premotor cortex, there was a decrease in the rate of exponential decay ($\Delta_{exponent}$ = −0.04 [−0.06, −0.02] dB), resulting in elevated broadband high-frequency activity (Fig. 5I). The changes in the 27- to 32-Hz and 54- to 60-Hz bands, as well as the aperiodic exponent, were significantly greater than those

Downloaded from https://www.science.org at Massachusetts Institute of Technology on October 26, 2023

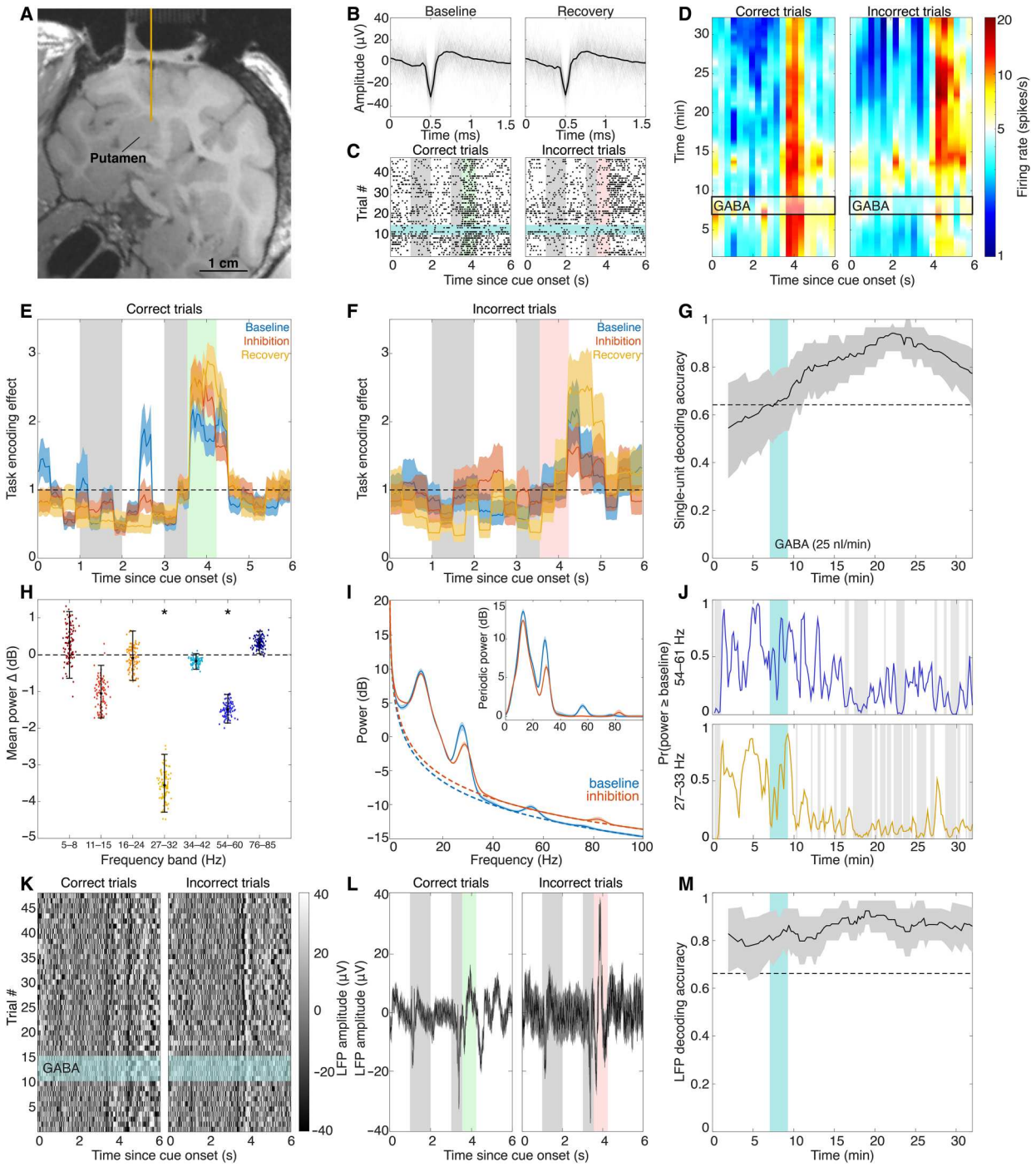

Fig. 5. The effects of intrastriatal GABA infusion on single-unit and LFP reward encoding in the putamen. (**A**) Magnetic resonance imaging (MRI) of the NHP subject in this study. The yellow line indicates the implantation trajectory of the fiber. (**B**) The waveform of single-unit activity was stable before and after GABA (25 nl/min) delivery. (**C**) Single-unit activity during correct and incorrect trials of the DMS task in Fig. 4 (B and C) (cyan shading, GABA infusion). (**D**) Single-unit firing rate varied within and between trials (black rectangle, GABA infusion). (**E** and **F**) The task encoding effect (a scaling factor for within-trial firing rate) during correct (E) and incorrect (F) trials varied between the baseline (blue), inhibition (red), and recovery (yellow) periods. (**G**) Decoding accuracy for correct versus incorrect trials was above the null (dashed line) after GABA was infused (gray shading, 95% confidence intervals; cyan shading, GABA infusion). (**H**) The change in mean LFP peak power between 10 min before and after GABA infusion. Asterisks indicate bands with changes significantly greater than observed in recordings without GABA infusions (fig. S15). (**I**) The mean and 95% confidence intervals for spectral power before (blue) and after (red) GABA. Dashed lines: Mean aperiodic component before and after GABA. Inset: Mean and 95% confidence intervals for the spectral power minus the aperiodic component. (**J**) The probability that peak power in the 27- to 32-Hz (yellow) and 54- to 60-Hz (blue) bands was greater than or equal to the peak power before GABA delivery. Periods where this probability was below 0.1 are shaded in gray. (**K**) LFP amplitude across trials. Cyan shading: GABA infusion. (**L**) The mean and 95% confidence intervals (gray shading) for LFP amplitude across trials. (**M**) Correct versus incorrect trial decoding accuracy using LFP observations was above the null (dashed line) throughout the experiment.

Downloaded from https://www.science.org at Massachusetts Institute of Technology on October 26, 2023

observed during putamen recordings with no infusions (fig. S15). Figure 5J shows the time course of the change in LFP oscillatory power in the 27- to 32-Hz and 54- to 60-Hz bands.

As in the premotor cortex, we found that, despite these changes in the oscillatory structure, task-evoked potentials were relatively stable throughout the experiment (Fig. 5K). Task-evoked LFP activity varied significantly between correct and incorrect trials (Fig. 5L), which enabled accurate decoding of correct and incorrect trials from LFP throughout the experiment (Fig. 5M and fig. S13). We did not find any significant changes in task performance compared to pre-GABA task performance (fig. S14).

DISCUSSION

Electrophysiological recording during pharmacological neuromodulation offers insight into causal roles of neurochemical signals in neuronal computation and behavior, promising to empower future diagnostics and therapies of neurological and psychiatric conditions. However, tools to enable such experiments in complex organisms, such as NHPs or human patients, remain scarce. To our knowledge, there has only been one study conducted more than two decades ago of near simultaneous iontophoretic drug delivery and electrophysiology in the striatum of an awake, behaving macaque (*58*). Notably, despite significant clinical interest in drug delivery to deep brain structures (*16*, *59*–*61*), physiological measures of the local effects of the drugs have been limited by the lack of available technologies. Large, stiff, or brittle devices pose significant safety risks to deep brain structures near life-sustaining vasculature (*62*). Our probe design overcomes these challenges by minimizing the fiber diameter and using flexible polymer, delivering autoclavable devices with significantly lower stiffness than state-of-the-art probes used for intracranial drug delivery experiments in NHPs (Fig. 1).

Multifunctional fibers enabled detailed investigation of the effect of local inhibition on cognitive neural encoding in both the cortex and putamen of an awake, behaving macaque. We found that, overall, GABA had the anticipated inhibitory effect on neuronal firing rates. Variability in the degree of inhibition reflects heterogeneity in GABA receptor expression, cellular excitability, and synaptic input (*47*, *48*, *63*). During the recovery period, we observed compensatory responses, with some neurons exhibiting higher firing rates than at baseline. We found that single-unit and LFP activity encoded task-related information even while firing rates were suppressed. Because of the highly redundant and flexible nature of the brain, we did not anticipate that unilateral intracortical microinfusions would affect behavior (*18*, *19*). By locally modulating neural excitability, we probed how information encoded in intact neural circuits adapts in the presence of changing neurochemical environment to maintain stable behavioral states (Figs. 4 and 5 and fig. S14).

In vivo neuromodulation affects neural dynamics across timescales ranging from seconds to hours. To characterize this broad dynamic range, we developed and implemented state-space models that offer millisecond, single-trial resolution of neural activity as it relates to behavior. First, we characterized the change in neuronal firing rate during and after local GABA infusion by estimating a state-space point process model of single-unit activity (Fig. 2). To gain detailed insight into how local GABA infusion affected neural computations, we developed a SS-GLM of firing rate variations within and across trials of the working memory task (Fig. 4). Application of this model revealed that encoding of cognitive task information by single units was not stationary and evolved throughout a period of temporary inhibition evoked by local GABA delivery. These results highlight that cognitive encoding by single units is dynamic (*8*, *64*) and can be altered by changes in local concentrations of neurotransmitters such as GABA.

We found that local drug delivery caused sustained changes in the oscillatory structure of LFP (Fig. 3). Local inhibition resulted in significant reduction of oscillatory power in the prominent beta and gamma frequency bands, each of which have been associated with cognitive function, including working memory (*4*, *43*, *54*). Despite changes in oscillatory content, task-evoked potentials provided a reliable signal for decoding task information, even during periods of near complete spike inhibition. Task-evoked LFP activity is associated with both local spiking and coordinated synaptic activity (*65*). We hypothesize that the primary contribution to task-evoked potentials was synaptic input from neural populations unaffected by local GABA infusions. Using multifunctional probes to investigate the relative contribution of local spiking and coordinated synaptic input would enable further exploration of this hypothesis.

In addition to empowering fundamental neuroscience, multifunctional fibers are poised to facilitate clinical research and disease management in patients. Intracranial drug delivery is used clinically for chemotherapy (*66*), gene therapy (*67*), and growth factor delivery (*68*). The current gold-standard probe implantation procedure relies on acquisition of magnetic resonance imaging (MRI) images throughout the surgery, which only provide coarse snapshots of the implantation process (*67*). Many microscale subcortical structures have characteristic electrophysiological signatures that can act as biomarkers for implantation trajectories (*69*–*72*). MRI-compatible multifunctional fibers with embedded electrodes (*36*) would improve MRI-guided neurosurgical procedures by offering real-time readout of probe location. Electrophysiology recordings can also reveal seizure foci (*62*), and infusion of inhibitory compounds through the same probe could facilitate termination or prevention of seizures (*16*). Given the broad range of translational opportunities for electrofluidic neurotechnology, our study in macaques provides a timely demonstration of the safety, sterility, and robustness of multifunctional fiber neurotechnology.

While the present study was limited to a single subject, our devices were designed to be compatible with commercially available microdrive systems and standard headstages, which will facilitate dissemination of this technology to the translational medicine and NHP neuroscience communities. Future device development will include extending the device functionality along the length of the fiber to increase electrode count and incorporating optical stimulation and recording (*36*, *37*, *39*). To further interrogate behavioral effects of neuromodulation, assemblies of fibers (fig. S1, E and F) could be used to deliver several submicroliter infusions across multiple locations, thereby modulating a large enough volume of cortex to elicit a behavioral response while maintaining stable electrophysiological recordings. Combined with state-space models designed to track neural dynamics over broad timescales, our multifunctional fibers will empower fundamental studies of neural computation in complex organisms and pave the way for clinical applications of neuromodulation and recording in patients.

Downloaded from https://www.science.org at Massachusetts Institute of Technology on October 26, 2023

MATERIALS AND METHODS

Study design

The goal of this study was to introduce fiber neurotechnology to the field of translational NHP neuroscience. We sought to empower neuroscientists by expanding the hardware and analysis toolboxes through the development of multifunctional fibers and state-space models of neural activity and demonstrating their synergy in a meaningful neurobiological context. We performed a controlled laboratory study to demonstrate that multifunctional fibers can simultaneously modulate and record neural activity in an awake macaque performing a working memory task. We expanded on data analysis methods that have been demonstrated to optimally characterize single-unit and LFP activity and demonstrated how their application could provide detailed measurements of the effects of localized modulation on cognitive neural activity. Our experimental demonstration was completed across 16 sessions in one macaque. Following the National Institutes of Health (NIH)'s *Guide for the Care and Use of Laboratory Animals*, we worked with the minimum number of animal subjects necessary to demonstrate device efficacy. The selected neuromodulatory compound, GABA, has a well-characterized inhibitory effect that is consistent across animals. Because neural activity can be variable in the absence of modulation, we replicated the infusion across multiple sessions to ensure that periods of inhibition were caused by GABA infusions and not coincidental. We completed vehicle control experiments with saline/aCSF to account for any mechanical effects of fluidic infusion and compared those effects to experiments with no infusions. Data from all sessions were included in this study; data preprocessing is described in detail in Supplementary Materials and Methods.

Device fabrication

We fabricated multifunctional fibers with four tungsten microelectrodes (25-μm diameter), two microfluidic channels [(49.9 ± 0.7) μm by (62.4 ± 0.8) μm], and a PEI (T_g = 217°C) cladding. Fiber diameter was tuned between 150 and 200 μm by varying the conditions of the thermal drawing process (Fig. 1), which has been previously described in detail (*36*, *37*, *73*). The fiber was then cut into 10-cm sections and connected to a custom backend interface.

Sterilization

All fiber and backend materials were selected to allow for autoclave sterilization of the devices. The connected devices were steam autoclaved at 121°C for 45 min. After assembly in the cranial grids (Supplementary Materials and Methods and Fig. 1F), the tips of the fibers were soaked in chlorhexidine diacetate (Novalsan) and rinsed with sterile water.

Animal experiments

All surgical and animal care procedures were approved by the Massachusetts Institute of Technology (MIT)'s Committee on Animal Care and were conducted in accordance with the guidelines of the NIH and MIT's Department of Comparative Medicine (protocol 0619-035-22). Experiments were conducted with one female macaque (*Macaca mulatta*, age of 21 years, weight of 9.3 kg). There were four ventral premotor cortex recordings with GABA microinfusions, four ventral premotor cortex recordings with saline or aCSF microinfusions, four ventral premotor cortex recordings with no microinfusions, one putamen recording with a GABA microinfusion, and three putamen recordings with no microinfusions. To compare neurophysiology over the course of microinfusion recordings, we define four periods: (i) the baseline period, before any fluid was delivered; (ii) the infusion period(s), during intracranial microinfusion(s); (iii) the inhibition period, 10 min following the last microinfusion; and (iv) the recovery period, greater than 20 min after microinfusion(s). To compare similar experimental periods in recordings without microinfusions, we consider two periods: (i) baseline, 0 to 10 min after the beginning of the recording; and (ii) after baseline, greater than 13 min following the beginning of the recording. Recordings were collected while the macaque performed a DMS task (Fig. 4) (*43*, *54*).

Statistics

Confidence interval notation

For variables where the quantity is expected to follow a Gaussian distribution, we report the means ± SEM. For other quantities, including those computed through bootstrap and Monte Carlo estimation (Supplementary Materials and Methods), we report the median [2.5th percentile, 97.5th percentile].

Estimating firing rate with point process models

To characterize the firing rate of single units, we model single-unit activity as a point process (*6*–*8*, *55*). For a given window of time, the probability of an action potential can be characterized with an instantaneous event rate parameter $\lambda(t)$. The instantaneous firing rate of a neuron is dependent on inherent properties, such as refractory periods and bursting properties, as well as external factors, like behavioral stimuli. Thus, we model single-unit activity with instantaneous spike rate conditioned on the underlying state of the unit using a point process model. The instantaneous rate of single-unit activity is characterized by the conditional intensity function

$$\lambda(t|X_t) = \lim_{\Delta \to 0} \frac{\Pr[N(t, t+\Delta)|X_t]}{\Delta}$$

where X_t refers to the state of the neuron at time t, which is influenced by spike history and other modulating factors. $N(t, t + \Delta)$ denotes the number of spikes in the interval $(t, t + \Delta]$, and $\Pr[N(t, t + \Delta)|X_t]$ is the probability of N spikes given the state at time t. The conditional intensity function $\lambda(t|X_t)$ characterizes a point process model of spiking activity, where inter-spike intervals are dependent on the underlying state of the unit.

We use two methods for characterizing single-unit firing rate over time. The first is a state-space point process model (*7*), where the sources of firing rate variation (e.g., spike history, encoding of behavioral information, and drug modulation) are characterized by a state variable x_t, which varies according to a Gaussian process model. The second method to model firing rate characterized both within-trial and across-trial dynamics. We use a SS-GLM approach to characterize the dynamic relationship between instantaneous firing rate, trial phase, and spike history (*8*, *55*).

To investigate task encoding between different trial variants, we further separated the training trials on the basis of which trial variant they belonged to (e.g., correct versus incorrect trials) and estimated a unique set of model parameters for each trial variant. The identity of a given test trial was decoded by comparing the deviance of the observed test data from each estimated model.

Downloaded from https://www.science.org at Massachusetts Institute of Technology on October 26, 2023

Time-frequency analysis of LFP oscillations

To compare awake LFP oscillatory structure before and after GABA or saline delivery, we characterized the LFP spectra using the FOOOF algorithm (*50*). The FOOOF algorithm models a given PSD as a sum of an aperiodic exponential decay component and Gaussian peaks for each periodic oscillation.

Characterizing task-evoked LFP

We modeled the relationship between LFP amplitude and trial epoch using an autoregressive model with trial covariates. To decode between trial variants from LFP, we used a similar method to the approach used for spike data. For a given test trial, we calculated the sum of squared error (SSE) between observed and predicted LFP from models trained with each trial variant and selected the trial variant with the lowest SSE.

Supplementary Materials

This PDF file includes:

Supplementary Materials and Methods
Figs. S1 to S16
References

REFERENCES AND NOTES

1. E. N. Brown, L. M. Frank, D. Tang, M. C. Quirk, M. A. Wilson, A statistical paradigm for neural spike train decoding applied to position prediction from ensemble firing patterns of rat hippocampal place cells. *J. Neurosci.* **18**, 7411–7425 (1998).
2. R. Desimone, T. D. Albright, C. G. Gross, C. Bruce, Stimulus-selective properties of inferior temporal neurons in the macaque. *J. Neurosci.* **4**, 2051–2062 (1984).
3. M. M. Churchland, J. P. Cunningham, M. T. Kaufman, J. D. Foster, P. Nuyujukian, S. I. Ryu, K. V. Shenoy, Neural population dynamics during reaching. *Nature* **487**, 51–56 (2012).
4. E. K. Miller, M. Lundqvist, A. M. Bastos, Working memory 2.0. *Neuron* **100**, 463–475 (2018).
5. O. G. Sani, Y. Yang, M. B. Lee, H. E. Dawes, E. F. Chang, M. M. Shanechi, Mood variations decoded from multi-site intracranial human brain activity. *Nat. Biotechnol.* **36**, 954–961 (2018).
6. W. Truccolo, U. T. Eden, M. R. Fellows, J. P. Donoghue, E. N. Brown, A point process framework for relating neural spiking activity to spiking history, neural ensemble, and extrinsic covariate effects. *J. Neurophysiol.* **93**, 1074–1089 (2005).
7. A. C. Smith, J. D. Scalon, S. Wirth, M. Yanike, W. A. Suzuki, E. N. Brown, State-space algorithms for estimating spike rate functions. *Comput. Intell. Neurosci.* **2010**, 1–14 (2010).
8. G. Czanner, U. T. Eden, S. Wirth, M. Yanike, W. A. Suzuki, E. N. Brown, Analysis of between-trial and within-trial neural spiking dynamics. *J. Neurophysiol.* **99**, 2672–2693 (2008).
9. F. R. Willett, D. T. Avansino, L. R. Hochberg, J. M. Henderson, K. V. Shenoy, High-performance brain-to-text communication via handwriting. *Nature* **593**, 249–254 (2021).
10. S. R. Nason, M. J. Mender, A. K. Vaskov, M. S. Willsey, N. Ganesh Kumar, T. A. Kung, P. G. Patil, C. A. Chestek, Real-time linear prediction of simultaneous and independent movements of two finger groups using an intracortical brain-machine interface. *Neuron* **109**, 3164–3177.e8 (2021).
11. D. L. Barack, E. K. Miller, C. I. Moore, A. M. Packer, L. Pessoa, L. N. Ross, N. C. Rust, A call for more clarity around causality in neuroscience. *Trends Neurosci.* **45**, 654–655 (2022).
12. M. M. Shanechi, Brain–machine interfaces from motor to mood. *Nat. Neurosci.* **22**, 1554–1564 (2019).
13. J. D. Heiss, D. P. Argersinger, W. H. Theodore, J. A. Butman, S. Sato, O. I. Khan, Convection-enhanced delivery of muscimol in patients with drug-resistant epilepsy. *Clin. Neurosurg.* **85**, E4–E15 (2019).
14. K. M. Tye, K. Deisseroth, Optogenetic investigation of neural circuits underlying brain disease in animal models. *Nat. Rev. Neurosci.* **13**, 251–266 (2012).
15. S. Tremblay, L. Acker, A. Afraz, D. L. Albaugh, H. Amita, A. R. Andrei, A. Angelucci, A. Aschner, P. F. Balan, M. A. Basso, G. Benvenuti, M. O. Bohlen, M. J. Caiola, R. Calcedo, J. Cavanaugh, Y. Chen, S. Chen, M. M. Chernov, A. M. Clark, J. Dai, S. R. Debes, K. Deisseroth, R. Desimone, V. Dragoi, S. W. Egger, M. A. G. Eldridge, H. G. El-Nahal, F. Fabbrini, F. Federer, C. R. Fetsch, M. G. Fortuna, R. M. Friedman, N. Fujii, A. Gail, A. Galvan, S. Ghosh, M. A. Gieselmann, R. A. Gulli, O. Hikosaka, E. A. Hosseini, X. Hu, J. Hüer, K. Inoue, R. Janz, M. Jazayeri, R. Jiang, N. Ju, K. Kar, C. Klein, A. Kohn, M. Komatsu, K. Maeda, J. C. Martinez-Trujillo, M. Matsumoto, J. H. R. Maunsell, D. Mendoza-Halliday, I. E. Monosov, R. S. Muers, L. Nurminen, M. Ortiz-Rios, D. J. O'Shea, S. Palfi, C. I. Petkov, S. Pojoga, R. Rajalingham, C. Ramakrishnan, E. D. Remington, C. Revsine, A. W. Roe, P. N. Sabes, R. C. Saunders, H. Scherberger, M. C. Schmid, W. Schultz, E. Seidemann, Y.-S. Senova, M. N. Shadlen, D. L. Sheinberg, C. Siu, Y. Smith, S. S. Solomon, M. A. Sommer, J. L. Spudich, W. R. Stauffer, M. Takada, S. Tang, A. Thiele, S. Treue, W. Vanduffel, R. Vogels, M. P. Whitmire, T. Wichmann, R. H. Wurtz, H. Xu, A. Yazdan-Shahmorad, K. V. Shenoy, J. J. DiCarlo, M. L. Platt, An open resource for non-human primate optogenetics. *Neuron* **108**, 1075–1090.e6 (2020).
16. J. D. Heiss, S. Walbridge, D. P. Argersinger, C. S. Hong, A. Ray-Chaudhury, R. R. Lonser, W. J. Elias, K. A. Zaghloul, Convection-enhanced delivery of muscimol into the bilateral subthalamic nuclei of nonhuman primates. *Neurosurgery* **84**, E420–E429 (2019).
17. N. P. Bichot, R. Xu, A. Ghadooshahy, M. L. Williams, R. Desimone, The role of prefrontal cortex in the control of feature attention in area V4. *Nat. Commun.* **10**, 5727 (2019).
18. A. J. Major, S. Vijayraghavan, S. Everling, Cholinergic overstimulation attenuates rule selectivity in macaque prefrontal cortex. *J. Neurosci.* **38**, 1137–1150 (2018).
19. S. Vijayraghavan, M. Wang, S. G. Birnbaum, G. V. Williams, A. F. T. Arnsten, Inverted-U dopamine D1 receptor actions on prefrontal neurons engaged in working memory. *Nat. Neurosci.* **10**, 376–384 (2007).
20. N. R. Herr, R. M. Wightman, Improved techniques for examining rapid dopamine signaling with iontophoresis. *Front. Biosci. (Elite Ed.)* **5**, 249–257 (2013).
21. B. Noudoost, T. Moore, A reliable microinjectrode system for use in behaving monkeys. *J. Neurosci. Methods* **194**, 218–223 (2011).
22. C. Dagdeviren, K. B. Ramadi, P. Joe, K. Spencer, H. N. Schwerdt, H. Shimazu, S. Delcasso, K. Amemori, C. Nunez-Lopez, A. M. Graybiel, M. J. Cima, R. Langer, Miniaturized neural system for chronic, local intracerebral drug delivery. *Sci. Transl. Med.* **10**, eaan2742 (2018).
23. M. I. Vanegas, K. R. Ubbard, R. Esfandyarpour, B. Noudoost, Microinjectrode system for combined drug infusion and electrophysiology. *J. Vis. Exp.*, e60365 (2019).
24. NeuroNexus, Electrode Arrays: Drug Delivery. Accessed Sept. 13, 2023; https://www.neuronexus.com/products/electrode-arrays/drug-delivery/
25. Plexon, Plexon U-Probe. Accessed Sept. 13, 2023; https://plexon.com/products/plexon-u-probe/
26. R. Chen, A. Canales, P. Anikeeva, Neural recording and modulation technologies. *Nat. Rev. Mater.* **2**, 16093 (2017).
27. G. Hong, C. M. Lieber, Novel electrode technologies for neural recordings. *Nat. Rev. Neurosci.* **20**, 330–345 (2019).
28. A. M. Stiller, B. J. Black, C. Kung, A. Ashok, S. F. Cogan, V. D. Varner, J. J. Pancrazio, A meta-analysis of intracortical device stiffness and its correlation with histological outcomes. *Micromachines (Basel)* **9**, 443 (2018).
29. C. Xie, J. Liu, T.-M. Fu, X. Dai, W. Zhou, C. M. Lieber, Three-dimensional macroporous nanoelectronic networks as minimally invasive brain probes. *Nat. Mater.* **14**, 1286–1292 (2015).
30. E. J. Welle, P. R. Patel, J. E. Woods, A. Petrossians, E. della Valle, A. Vega-Medina, J. M. Richie, D. Cai, J. D. Weiland, C. A. Chestek, Ultra-small carbon fiber electrode recording site optimization and improved *in vivo* chronic recording yield. *J. Neural Eng.* **17**, 026037 (2020).
31. J. Gurke, T. E. Naegele, S. Hilton, R. Pezone, V. F. Curto, D. G. Barone, E. J. W. List-Kratochvil, A. Carnicer-Lombarte, G. G. Malliaras, Hybrid fabrication of multimodal intracranial implants for electrophysiology and local drug delivery. *Mater. Horiz.* **9**, 1727–1734 (2022).
32. J. W. Jeong, J. G. McCall, G. Shin, Y. Zhang, R. Al-Hasani, M. Kim, S. Li, J. Y. Sim, K. I. Jang, Y. Shi, D. Y. Hong, Y. Liu, G. P. Schmitz, L. Xia, Z. He, P. Gamble, W. Z. Ray, Y. Huang, M. R. Bruchas, J. A. Rogers, Wireless optofluidic systems for programmable in vivo pharmacology and optogenetics. *Cell* **162**, 662–674 (2015).
33. A. Vázquez-Guardado, Y. Yang, A. J. Bandodkar, J. A. Rogers, Recent advances in neurotechnologies with broad potential for neuroscience research. *Nat. Neurosci.* **23**, 1522–1536 (2020).
34. J. A. Frank, M. J. Antonini, P. Anikeeva, Next-generation interfaces for studying neural function. *Nat. Biotechnol.* **37**, 1013–1023 (2019).
35. C.-H. Chiang, S. M. Won, A. L. Orsborn, K. J. Yu, M. Trumpis, B. Bent, C. Wang, Y. Xue, S. Min, V. Woods, C. Yu, B. H. Kim, S. B. Kim, R. Huq, J. Li, K. J. Seo, F. Vitale, A. Richardson, H. Fang, Y. Huang, K. Shepard, B. Pesaran, J. A. Rogers, J. Viventi, Development of a neural interface for high-definition, long-term recording in rodents and nonhuman primates. *Sci. Transl. Med.* **12**, eaay4682 (2020).
36. M. Antonini, A. Sahasrabudhe, A. Tabet, M. Schwalm, D. Rosenfeld, I. Garwood, J. Park, G. Loke, T. Khudiyev, M. Kanik, N. Corbin, A. Canales, A. Jasanoff, Y. Fink, P. Anikeeva, Customizing MRI-compatible multifunctional neural interfaces through fiber drawing. *Adv. Funct. Mater.* **31**, 2104857 (2021).
37. A. Canales, X. Jia, U. P. Froriep, R. A. Koppes, C. M. Tringides, J. Selvidge, C. Lu, C. Hou, L. Wei, Y. Fink, P. Anikeeva, Multifunctional fibers for simultaneous optical, electrical and chemical interrogation of neural circuits in vivo. *Nat. Biotechnol.* **33**, 277–284 (2015).

Downloaded from https://www.science.org at Massachusetts Institute of Technology on October 26, 2023

38. J. A. Frank, M. J. Antonini, P. H. Chiang, A. Canales, D. B. Konrad, I. C. Garwood, G. Rajic, F. Koehler, Y. Fink, P. Anikeeva, In vivo photopharmacology enabled by multifunctional fibers. *ACS Chem. Nerosci.* **11**, 3802–3813 (2020).
39. S. Park, Y. Guo, X. Jia, H. K. Choe, B. Grena, J. Kang, J. Park, C. Lu, A. Canales, R. Chen, Y. S. Yim, G. B. Choi, Y. Fink, P. Anikeeva, One-step optogenetics with multifunctional flexible polymer fibers. *Nat. Neurosci.* **20**, 612–619 (2017).
40. M. Matsumura, T. Sawaguchi, GABAergic inhibition of neuronal activity in the primate motor and premotor cortex during voluntary movement. *J. Neurophysiol.* **68**, 692–702 (1992).
41. J. M. Hupé, G. Chouvet, J. Bullier, Spatial and temporal parameters of cortical inactivation by GABA. *J. Neurosci. Methods* **86**, 129–143 (1999).
42. L. D. Liu, K. D. Miller, C. C. Pack, A unifying motif for spatial and directional surround suppression. *J. Neurosci.* **38**, 989–999 (2018).
43. A. M. Bastos, R. Loonis, S. Kornblith, M. Lundqvist, E. K. Miller, Laminar recordings in frontal cortex suggest distinct layers for maintenance and control of working memory. *Proc. Natl. Acad. Sci. U.S.A.* **115**, 1117–1122 (2018).
44. M. Lundqvist, P. Herman, M. R. Warden, S. L. Brincat, E. K. Miller, Gamma and beta bursts during working memory readout suggest roles in its volitional control. *Nat. Commun.* **9**, 394 (2018).
45. M. Haruno, M. Kawato, Different neural correlates of reward expectation and reward expectation error in the putamen and caudate nucleus during stimulus-action-reward association learning. *J. Neurophysiol.* **95**, 948–959 (2006).
46. Y. Yu, T. H. B. FitzGerald, K. J. Friston, Working memory and anticipatory set modulate midbrain and putamen activity. *J. Neurosci.* **33**, 14040–14047 (2013).
47. Y. Kanemoto, M. Matsuzaki, S. Morita, T. Hayama, J. Noguchi, N. Senda, A. Momotake, T. Arai, H. Kasai, Spatial distributions of GABA receptors and local inhibition of Ca2+ transients studied with GABA uncaging in the dendrites of CA1 pyramidal neurons. *PLOS ONE* **6**, e22652 (2011).
48. C. Piette, M. Vandecasteele, C. Bosch-Bouju, V. Goubard, V. Paillé, Y. Cui, A. Mendes, S. Perez, S. Valtcheva, H. Xu, P. Pouget, L. Venance, Intracellular properties of deep-layer pyramidal neurons in frontal eye field of macaque monkeys. *Front. Synaptic Neurosci.* **13**, 725880 (2021).
49. G. Buzsáki, C. A. Anastassiou, C. Koch, The origin of extracellular fields and currents—EEG, ECoG, LFP and spikes. *Nat. Rev. Neurosci.* **13**, 407–420 (2012).
50. T. Donoghue, M. Haller, E. J. Peterson, P. Varma, P. Sebastian, R. Gao, T. Noto, A. H. Lara, J. D. Wallis, R. T. Knight, A. Shestyuk, B. Voytek, Parameterizing neural power spectra into periodic and aperiodic components. *Nat. Neurosci.* **23**, 1655–1665 (2020).
51. R. Gao, E. J. Peterson, B. Voytek, Inferring synaptic excitation/inhibition balance from field potentials. *Neuroimage* **158**, 70–78 (2017).
52. Y. Sun, Y. Yang, V. C. Galvin, S. Yang, A. F. Arnsten, M. Wang, Nicotinic α4β2 cholinergic receptor influences on dorsolateral prefrontal cortical neuronal firing during a working memory task. *J. Neurosci.* **37**, 5366–5377 (2017).
53. W. F. Asaad, G. Rainer, E. K. Miller, Task-specific neural activity in the primate prefrontal cortex. *J. Neurophysiol.* **84**, 451–459 (2000).
54. A. M. Bastos, M. Lundqvist, A. S. Waite, N. Kopell, E. K. Miller, Layer and rhythm specificity for predictive routing. *Proc. Natl. Acad. Sci. U.S.A.* **117**, 31459–31469 (2020).
55. U. T. Eden, L. M. Frank, R. Barbieri, V. Solo, E. N. Brown, Dynamic analysis of neural encoding by point process adaptive filtering. *Neural Comput.* **16**, 971–998 (2004).
56. K. A. Lowe, W. Zinke, J. D. Cosman, J. D. Schall, Frontal eye fields in macaque monkeys: Prefrontal and premotor contributions to visually guided saccades. *Cereb. Cortex* **32**, 5083–5107 (2022).
57. S. Laquitaine, C. Piron, D. Abellanas, Y. Loewenstein, T. Boraud, Complex population response of dorsal putamen neurons predicts the ability to learn. *PLOS ONE* **8**, e80683 (2013).
58. M. Inase, B. M. Li, J. Tanji, Dopaminergic modulation of neuronal activity in the monkey putamen through D1 and D2 receptors during a delayed Go/Nogo task. *Exp. Brain Res.* **117**, 207–218 (1997).
59. D. Yin, R. M. Richardson, M. S. Fiandaca, J. Bringas, J. Forsayeth, M. S. Berger, K. S. Bankiewicz, Cannula placement for effective convection-enhanced delivery in the nonhuman primate thalamus and brainstem: Implications for clinical delivery of therapeutics. *J. Neurosurg.* **113**, 240–248 (2010).
60. M. Luz, P. C. Allen, J. Bringas, C. Boiko, D. E. Stockinger, K. J. Nikula, O. Lewis, M. Woolley, H. C. Fibiger, K. Bankiewicz, E. Mohr, Intermittent convection-enhanced delivery of GDNF into rhesus monkey putamen: Absence of local or cerebellar toxicity. *Arch. Toxicol.* **92**, 2353–2367 (2018).
61. X. Fan, B. D. Nelson, Y. Ai, D. K. Stiles, D. M. Gash, P. A. Hardy, Z. Zhang, Continuous intraputamenal convection-enhanced delivery in adult rhesus macaques. *J. Neurosurg.* **123**, 1569–1577 (2015).
62. V. N. Vakharia, R. Sparks, R. Rodionov, S. B. Vos, C. Dorfer, J. Miller, D. Nilsson, M. Tisdall, S. Wolfsberger, A. W. McEvoy, A. Miserocchi, G. P. Winston, A. G. O'Keeffe, S. Ourselin, J. S. Duncan, Computer-assisted planning for the insertion of stereoelectroencephalography electrodes for the investigation of drug-resistant focal epilepsy: An external validation study. *J. Neurosurg.* **130**, 1–10 (2018).
63. E. A. Kiyatkin, G. V. Rebec, Modulation of striatal neuronal activity by glutamate and GABA: Iontophoresis in awake, unrestrained rats. *Brain Res.* **822**, 88–106 (1999).
64. S. A. Allsop, R. Wichmann, F. Mills, A. Burgos-Robles, C. J. Chang, A. C. Felix-Ortiz, A. Vienne, A. Beyeler, E. M. Izadmehr, G. Glober, M. I. Cum, J. Stergiadou, K. K. Anandalingam, K. Farris, P. Namburi, C. A. Leppla, J. C. Weddington, E. H. Nieh, A. C. Smith, D. Ba, E. N. Brown, K. M. Tye, Corticoamygdala transfer of socially derived information gates observational learning. *Cell* **173**, 1329–1342.e18 (2018).
65. G. Buzsáki, X.-J. Wang, Mechanisms of gamma oscillations. *Annu. Rev. Neurosci.* **35**, 203–225 (2012).
66. R. S. D'Amico, M. K. Aghi, M. A. Vogelbaum, J. N. Bruce, Convection-enhanced drug delivery for glioblastoma: A review. *J. Neurooncol* **151**, 415–427 (2021).
67. V. Sudhakar, R. M. Richardson, Gene therapy for neurodegenerative diseases. *Neurotherapeutics* **16**, 166–175 (2019).
68. A. M. Mehta, A. M. Sonabend, J. N. Bruce, Convection-enhanced delivery. *Neurotherapeutics* **14**, 358–371 (2017).
69. N. Koirala, L. Serrano, S. Paschen, D. Falk, A. R. Anwar, P. Kuravi, G. Deuschl, S. Groppa, M. Muthuraman, Mapping of subthalamic nucleus using microelectrode recordings during deep brain stimulation. *Sci. Rep.* **10**, 19241 (2020).
70. H. S. Venkatesh, W. Morishita, A. C. Geraghty, D. Silverbush, S. M. Gillespie, M. Arzt, L. T. Tam, C. Espenel, A. Ponnuswami, L. Ni, P. J. Woo, K. R. Taylor, A. Agarwal, A. Regev, D. Brang, H. Vogel, S. Hervey-Jumper, D. E. Bergles, M. L. Suvà, R. C. Malenka, M. Monje, Electrical and synaptic integration of glioma into neural circuits. *Nature* **573**, 539–545 (2019).
71. S. Oxenford, J. Roediger, C. Neudorfer, L. Milosevic, C. Güttler, P. Spindler, P. Vajkoczy, W. J. Neumann, A. Kühn, A. Horn, Lead-OR: A multimodal platform for deep brain stimulation surgery. *eLife* **11**, e72929 (2022).
72. K. J. Miller, T. Prieto, N. R. Williams, C. H. Halpern, Case studies in neuroscience: The electrophysiology of a human obsession in nucleus accumbens. *J. Neurophysiol.* **121**, 2336–2340 (2019).
73. G. Loke, W. Yan, T. Khudiyev, G. Noel, Y. Fink, Recent progress and perspectives of thermally drawn multimaterial fiber electronics. *Adv. Mater.* **32**, e1904911 (2020).
74. K. S. Saleem, N. K. Logothetis, *A Combined MRI and Histology Atlas of the Rhesus Monkey Brain in Stereotaxic Coordinates* (Academic Press, 2012).
75. D. A. Leopold, N. K. Logothetis, Spatial patterns of spontaneous local field activity in the monkey visual cortex. *Rev. Neurosci.* **14**, 195–205 (2003).
76. Z. Chen, S. Vijayan, R. Barbieri, M. A. Wilson, E. N. Brown, Discrete- and continuous-time probabilistic models and algorithms for inferring neuronal UP and DOWN states. *Neural Comput.* **21**, 1797–1862 (2009).
77. L. L. Chen, R. Madhavan, B. I. Rapoport, W. S. Anderson, Real-time brain oscillation detection and phase-locked stimulation using autoregressive spectral estimation and time-series forward prediction. *IEEE Trans. Biomed. Eng.* **60**, 753–762 (2013).

Acknowledgments: This work made use of the shared equipment at the Center for Materials Science and Engineering supported by the National Science Foundation (NSF) (DMR-1419807) and the Institute for Soldier Nanotechnologies (U.S. Army Research Office, W911NF-13-D-000). **Funding:** This work was supported in part by the following funding sources: McGovern Institute for Brain Research (MINT grant, P.A.); the JPB Foundation (E.N.B. and E.K.M.); National Institute for Neurological Disorders and Stroke (NINDS, R01-NS115025, P.A.); NSF Center for Neurotechnology (EEC-1028725, P.A.); National Institutes of Health (NIH; P01-GM118629, E.N.B. and E.K.M.; 5T32EB019940-05, I.C.G.); Office of Naval Research, N00014-22-1-2453 (E.K.M); and National Institute of Mental Health, 1R01MH131715-01 (E.K.M.). I.C.G. is a recipient of the NSF Graduate Research Fellowship and Mathworks Fellowship. A.J.M. is a recipient of the Simons Center for the Social Brain Postdoctoral Fellowship. A.S. is a recipient of the Lore Harp McGovern Fellowship. M.-J.A. is a recipient of the Friends of McGovern Graduate Fellowship. Y.L. is a recipient of a scholarship from the Kwanjeong Educational Foundation. **Author contributions:** Conceptualization: I.C.G., A.J.M., E.K.M., E.N.B., and P.A. Methodology: I.C.G., A.J.M., M.-J.A., J.C., Y.L., A.S., M.K.M., E.K.M., E.N.B., and P.A. Investigation: I.C.G. and A.J.M. Visualization: I.C.G., M.-J.A., J.C., and P.A. Funding acquisition: E.K.M., E.N.B., and P.A. Project administration: M.K.M., E.K.M., E.N.B., and P.A. Supervision: E.K.M., E.N.B., and P.A. Writing—original draft: I.C.G., A.J.M., M.-J.A., E.N.B., and P.A. Writing—review and editing: I.C.G., A.J.M., M.-J.A., J.C., M.K.M., E.K.M., E.N.B., and P.A. **Competing interests:** P.A. and M.-J.A. are cofounders of NeuroBionics, a start-up company that seeks to commercialize fiber technology conceptually similar to the fibers reported here for medical use. E.N.B. has licensed intellectual property to Masimo for the analysis of EEG under anesthesia. E.N.B. is a cofounder of PASCALL, a company constructing control systems for anesthesia. The other authors declare that they have no competing

Downloaded from https://www.science.org at Massachusetts Institute of Technology on October 26, 2023

interests. **Data and materials availability:** All data needed to evaluate the conclusions in the paper are present in the paper and/or the Supplementary Materials. Additional data and code are available on Dryad (DOI: 10.5061/dryad.zkh1893ft) and GitHub (https://github.com/igarwood/NHP_fibers). Physical samples of multifunctional fibers are available from the corresponding author (P.A.) upon reasonable request.

Submitted 9 February 2023
Accepted 5 September 2023
Published 6 October 2023
10.1126/sciadv.adh0974

Downloaded from https://www.science.org at Massachusetts Institute of Technology on October 26, 2023

ScienceAdvances

Multifunctional fibers enable modulation of cortical and deep brain activity during cognitive behavior in macaques

Indie C. Garwood, Alex J. Major, Marc-Joseph Antonini, Josefina Correa, Youngbin Lee, Atharva Sahasrabudhe, Meredith K. Mahnke, Earl K. Miller, Emery N. Brown, and Polina Anikeeva

Sci. Adv. **9** (40), eadh0974. DOI: 10.1126/sciadv.adh0974

View the article online
https://www.science.org/doi/10.1126/sciadv.adh0974
Permissions
https://www.science.org/help/reprints-and-permissions

Downloaded from https://www.science.org at Massachusetts Institute of Technology on October 26, 2023

Use of this article is subject to the Terms of service

Science Advances (ISSN 2375-2548) is published by the American Association for the Advancement of Science. 1200 New York Avenue NW, Washington, DC 20005. The title *Science Advances* is a registered trademark of AAAS.

Copyright © 2023 The Authors, some rights reserved; exclusive licensee American Association for the Advancement of Science. No claim to original U.S. Government Works. Distributed under a Creative Commons Attribution NonCommercial License 4.0 (CC BY-NC).